***Supplementary Information*:**

Micro-/Nanoparticle Separation Combining Inertial and Thermophoretic Effects in Three-dimensional Serpentine-Spiral Channels

Junho Kim[1], Hwisu Jeon[1], Kyunghun Lee[1], and Taesung Kim[1,2]*

[1]Department of Mechanical Engineering, Ulsan National Institute of Science and Technology (UNIST), 50 UNIST-Gil, Ulsan 44919, Republic of Korea.

[2]Department of Biomedical Engineering, Ulsan National Institute of Science and Technology (UNIST), 50 UNIST-Gil, Ulsan 44919, Republic of Korea.

[*]Correspondence

Taesung Kim

Department of Mechanical Engineering

Ulsan National Institute of Science and Technology (UNIST)

50 UNIST-gil, Ulsan 44919, Republic of Korea

E-mail: tskim@unist.ac.kr

Tel: +82-52-217-2313

Fax: +82-52-217-2409

Supplementary Notes

Note S1: Dimension and fabrication of the microfluidic device

Using standard photolithography and deep reactive ion etching processes, a silicon master mold was fabricated (Figure S1). The circular pillars have a diameter of 300 μm and a depth of 400 μm (including the spacer), with an inter-pillar spacing of 1200 μm, and the serpentine unit has a length (L) of 21 mm (refer to Figure 1b). The distance between the observation window in the outlet region and the channel sidewall is 300 μm. Subsequently, a PDMS mold was fabricated using standard soft lithography, and the chip was assembled by bonding the Ostemer channel layer with the Ostemer cover film. The cover film, with a thickness of 100 μm, was prepared by spin-coating the resin at 800 rpm for 30 seconds. A UV lamp (30 W, 365 nm) was used for photopolymerization. The channel layer was cured with the glass-facing side in direct contact with the UV lamp, whereas the cover film was cured at approximately 60 mm from the lamp, exposing the resin directly to UV light. During the final bonding step, UV exposure was applied from the PET side of the cover film. After all UV curing steps, the assembled chips underwent thermal curing in a convection oven at 65°C for 24 hours. The open region of the heating rod was conformally bonded using double-coated tissue tape, while the exposed areas on the sidewalls (except for the observation window) were completely sealed with epoxy adhesive. The vertical patterns observed on the sidewalls under an optical microscope, as shown in Figure S3, are a result of sidewall roughness formed by the film-coated mask (FCG) during the photolithography process. Moreover, these patterns were replicated through the DRIE process, and additionally, the scallop patterns produced by the BOSCH process cycle were approximately 30 nm in size. The microfluidic effects induced by these patterns are negligible at the flow rates used in this work ($0.1 < Re < 50$)[1].

Note S2: Thermodiffusion coefficient (D_T) of charged particles

The thermal diffusion coefficient, D_T which defines the Soret coefficient, can be decomposed into two additive contributions[2, 3]: the hydration-entropy effect at the particle–liquid interface and the ionic-shielding effect within the electric double layer (EDL):

$$D_T = D_{T,hyd} + D_{T,ionic} \tag{S1}$$

Hydration-entropy contribution

$$D_{T,hyd} = -\frac{d}{3\mu} s_{hyd} \tag{S2}$$

where d is the particle diameter, μ is fluid viscosity, and s_{hyd} is the hydration entropy per unit interfacial area. Because our measurements inevitably included inertial drift, we cannot isolate the influence of D_T directly. Consequently, we adopt $s_{hyd} = 1.6 \times 10^{-8}\, J/m^2K$, which was reported for a system with a comparable temperature gradient and mean fluid temperature (e.g., 45.2°C)[4].

Ionic-shielding contribution

For a thin EDL with a Debye length of $\lambda_D = 1/\kappa$, which corresponds to $\lambda_D = 9.6\, nm$ for an ionic strength of 0.11 mM, thermal diffusion coefficient due to ionic shielding $D_{T,ionic}$ simplifies to:

$$D_{T,ionic} = \frac{\epsilon \zeta^2}{12\mu T} \kappa d (1 - \tau) \tag{S3}$$

where ε is the fluid permittivity, T is the fluid temperature, and ζ is the zeta potential of particles. Zeta potentials were measured using a Zetasizer Nano. The dispersant settings were water for particles and PBS 1X for cells. Under identical solution conditions, the zeta potentials of cells in the culture media and PBS 1X were similar, whereas the zeta potential of particles increased markedly in the SDS/NaCl mixture. Finally, the dimensionless parameter ($\tau = -1.34$) was chosen to match the reported value for water, which relates temperature and permittivity[5]. The thermophoretic migration directions for all particle sizes were confirmed experimentally (Figures 3 – 5).

Note S3: Comparison of acting forces

Figure S5 shows theoretical calculations of the multi-physical forces. Inertial forces arising from Dean flow—generated by the spiral geometry implemented in SART—exceeded shear-gradient lift by two orders of magnitude at the experimental Reynolds numbers used in this work. As a result, inertial focusing of 4.9 μm particles would be expected to be weak, yet fully developed inertial focusing appears from *Re* = 3.75 onward (Figure S6). This can be attributed to transient, wall-directed secondary flows in the height direction of the channel that arise as particles traverse the serpentine unit, promoting inertial equilibrium. In Figure S5b, the contribution of Dean drag is indicated by a hatched line (representing the maximum Dean drag force), and the equilibrium position determined by the lift-coefficient vector should also be considered[6].

When thermophoretic effects are added, microparticles reach their equilibrium positions more rapidly and form narrower focusing bands (Figure S7). Under the combined action of inertial lift and thermophoretic drift, microparticles concentrate near the inner wall, whereas nanoparticles settle into an equilibrium region near the outer wall due to the combined influence of inertial, thermophoretic, and wall-interaction forces.

Note S4: Multi-physics numerical simulation and governing equations

Numerical simulations were conducted using COMSOL Multiphysics (version 5.3a; COMSOL Inc., Sweden). The governing equations included the Navier–Stokes equation with continuity, the energy conservation equation, and the Nernst–Planck equation as follows:

$$\rho\frac{\partial \boldsymbol{u}}{\partial t} + \rho(\boldsymbol{u}\cdot\nabla)\boldsymbol{u} = \nabla\cdot\left[-p\boldsymbol{I} + \mu\left(\nabla\boldsymbol{u} + (\nabla\boldsymbol{u})^{T}\right)\right] \tag{S4}$$

$$\rho\nabla\cdot\boldsymbol{u} = 0 \tag{S5}$$

$$\rho C_p u\cdot\nabla T + \nabla\cdot q = 0 \tag{S6}$$

$$J_i = c_i u - D_i\nabla c_i - \frac{D_i z_i F c_i}{RT}\nabla\phi - D_{T,i}c_i\nabla T \tag{S7}$$

where ρ, $\boldsymbol{u}$, p, z_i, J_i, c_i, D_i, $D_{T,i}$, F, R, and ϕ are the density, velocity vector, pressure of the fluid/electrolyte, valency, molar flux, concentration, diffusion coefficient, thermal diffusion coefficient of the ionic species i, Faraday constant, universal gas constant, and electric potential, respectively. Ostemer channel walls were modeled with thermal properties typical of epoxy-based polymers (thermal conductivity k = 0.2 W/m·K). Fluid properties were assumed equivalent to pure water with 100 mM NaCl; SDS effects were neglected. The initial temperature of the numerical simulation domain was set to 25 °C. Diffusion coefficients for Na^+ and Cl^- under these conditions were set to $D_{Na} = 1.33 \times 10^{-9}$ m²/s and $D_{Cl} = 2.03 \times 10^{-9}$ m²/s. Flow and thermal boundary conditions matched experimental settings: the inlet flow corresponded to Re = 2.14 and the wall temperatures were fixed at T_H = 90 °C and T_L = 20 °C. No external electric field was applied. The multi-physic simulation resulted in steady-state concentration gradients of 99.7 mM < [Na^+] < 100.3 mM and 99.3 mM < [Cl^-] < 100.6 mM.

Note S5: Enhanced particle drift by induced electric fields

To assess the electric field generated by the ion concentration gradients arising from coupled multi-physical effects, the previously calculated steady-state gradients were substituted into the Nernst equation:

$$\phi_i = \frac{RT}{z_i F} \ln\left(\frac{c_{i,hot}}{c_{i,cold}}\right) \tag{S8}$$

$$E = -\nabla\phi = -\frac{\sum_i D_i \phi_i}{\sum_i D_i} \cdot \frac{1}{L} \tag{S9}$$

The resulting electric field was E = -4.1 mV/cm, oriented from the colder side toward the hotter side of the channel. This electric field originates from the unequal thermal transport of individual ions ($Q_+ > Q_-$), a behavior that closely matches trends reported in prior studies[7, 8]. Accordingly, this Nernst-derived electric field is expected to contribute to the net thermophoretic drift of particles in

agreement with the literature. All supplementary figures and theoretical derivations correspond directly to the data presented in the main manuscript, and provide additional detail on device fabrication, thermophoretic modeling, and force analysis.

Supplementary Figures

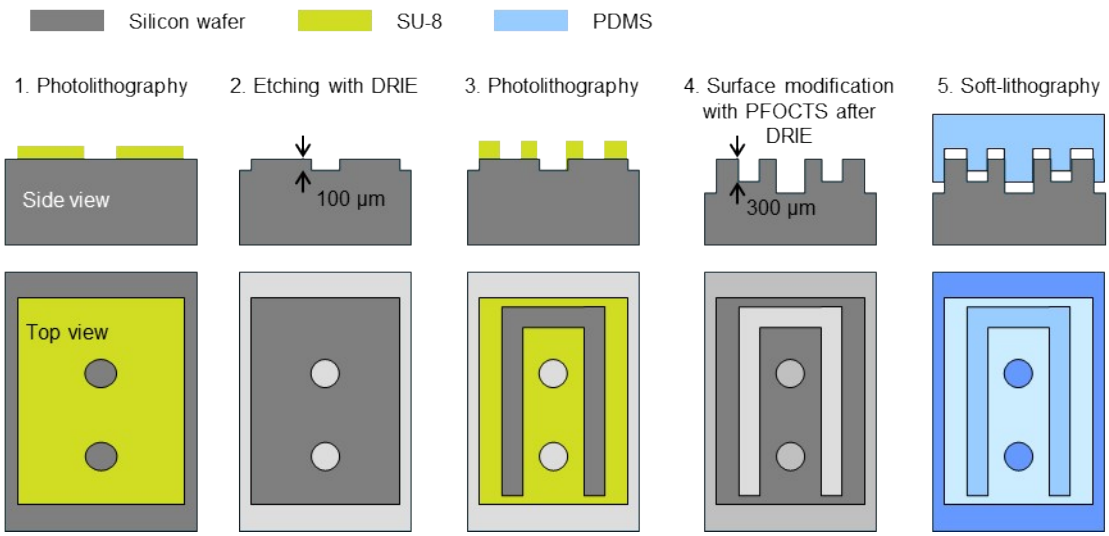

Figure S1. Schematic illustration of the multilayer microchannel fabrication process using a silicon master mold and a PDMS mold. The fabrication steps include (1) patterning of micropillar templates on the SU-8 master mold; (2) generation of three-dimensional microstructures with varying depths (~300 µm) using DRIE; (3) patterning of a secondary layer to define microfluidic channels; (4) surface modification with PFOCTS; (5) replication of a PDMS device via soft-lithograph. The side and top views illustrate the structural complexity and fluidic layout. Color coding: gray – silicon wafer; yellow green – SU-8 photoresist; light blue – PDMS.

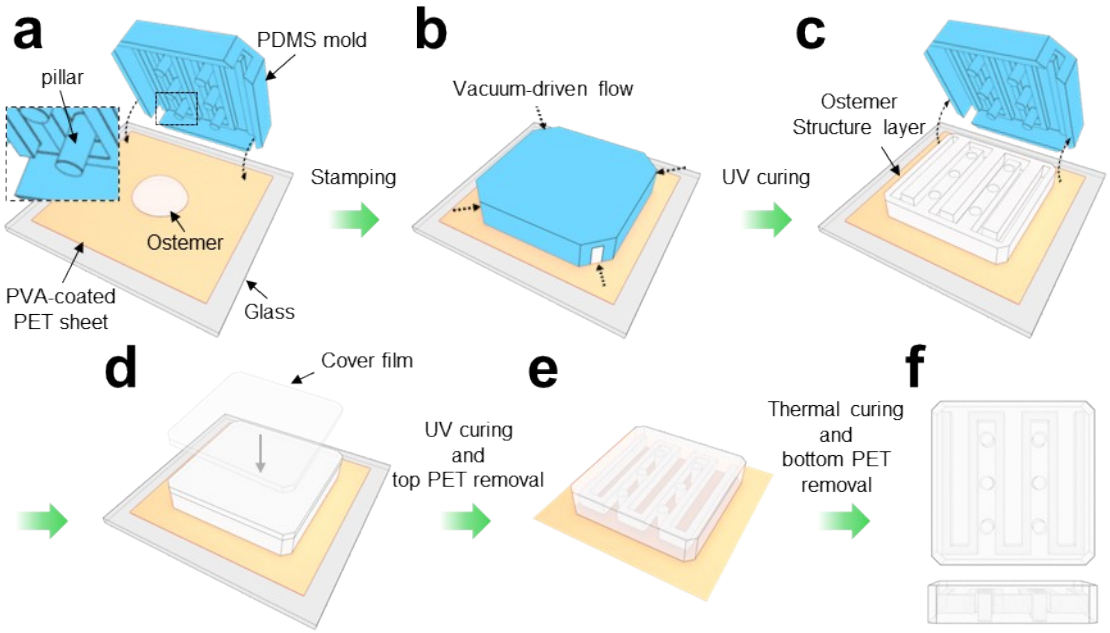

Figure S2. Fabrication of the multilayer microfluidic chip using an Ostemer replication process. (a) Dropping an Ostemer droplet onto a PVA spin-coated PET sheet, followed by stamping with a degassed PDMS mold supported by the mold pillars. (b) Formation of a tight seal between the PDMS mold and the PET sheet, maintained for 30 minutes to remove air bubbles, followed by UV curing for 5 minutes. (c) Removal of the PDMS mold from the Ostemer structure layer. (d) Bonding of the UV-cured Ostemer cover film (3 minutes) to the Ostemer structure layer, with subsequent removal of the glass substrate. (e) Final UV curing for 3 minutes, thermal curing for 1 day, and detachment of the PET sheet from the fully cured Ostemer chip. (f) The front and top views of the fabricated Ostemer chip reveal the integrated microstructures replicated from the original mold.

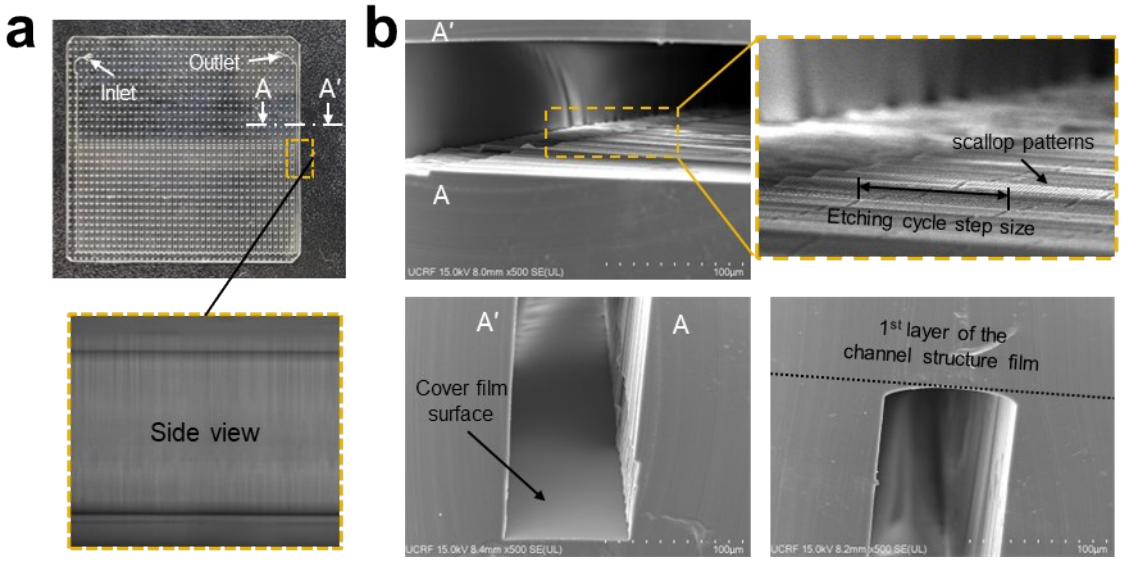

Figure S3. Images of the Ostemer chip used in the SART device. (a) Photograph of the full Ostemer chip, showing the inlet, outlet, and densely packed channel network. (b) Cross-sectional SEM images of the Ostemer chip along the A – A' line reveal the strong bonding between the channel structure layer and the cover film. High-magnification SEM image shows the scallop patterns on the sidewalls, generated by the DRIE process, with clearly defined etching cycle step sizes. Additional SEM views demonstrate the smooth surface of the cover film, the interface between microchannel layers, and the structural integrity of the replicated 3D profile.

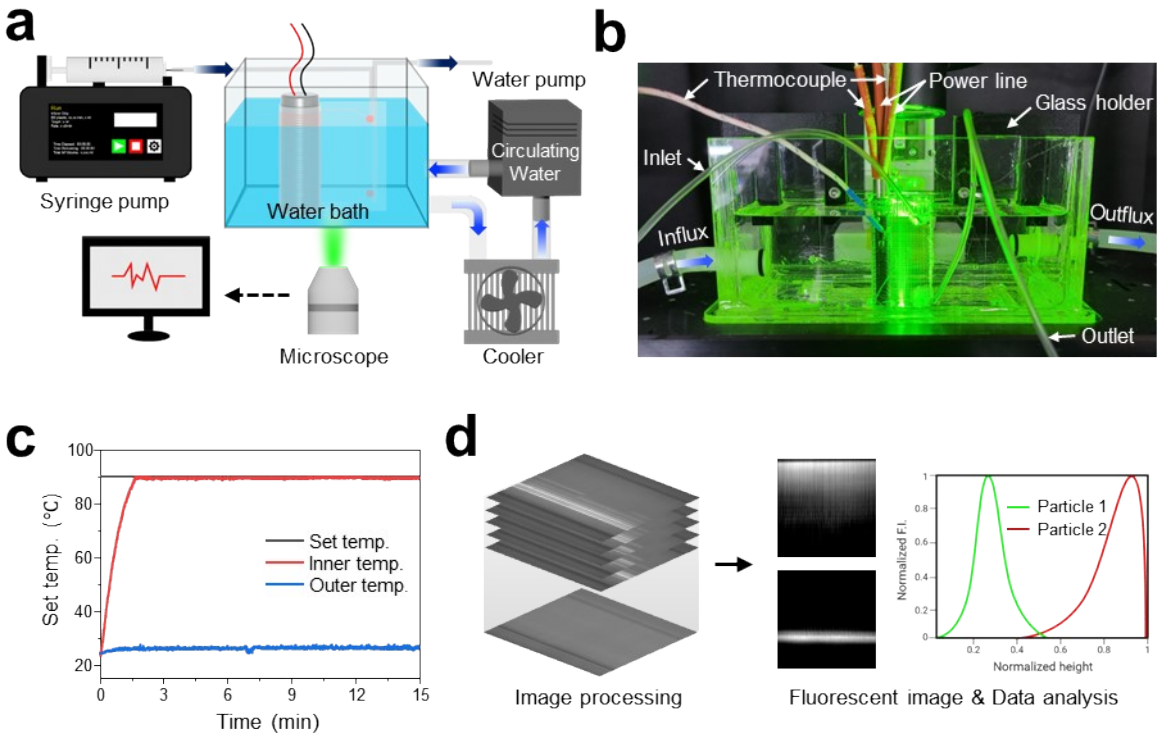

Figure S4. Experimental setup and characterization of the thermal operation and image processing in the SART device. (a) Schematic diagram of the experimental system, including syringe-driven flow and a water bath with a recirculating cooling loop for temperature control. (b) Photograph of the assembled SART device during operation, showing the inlet/outlet tubing, thermocouple, power line, and the glass holder configuration. (c) Plot demonstrating thermal stability of the system, where the internal heater temperature was maintained at 90 °C while the outer wall remained at ~23 °C. (d) Overview of the image processing steps for analyzing fluorescent particle distributions, including image stacking and fluorescence intensity quantification.

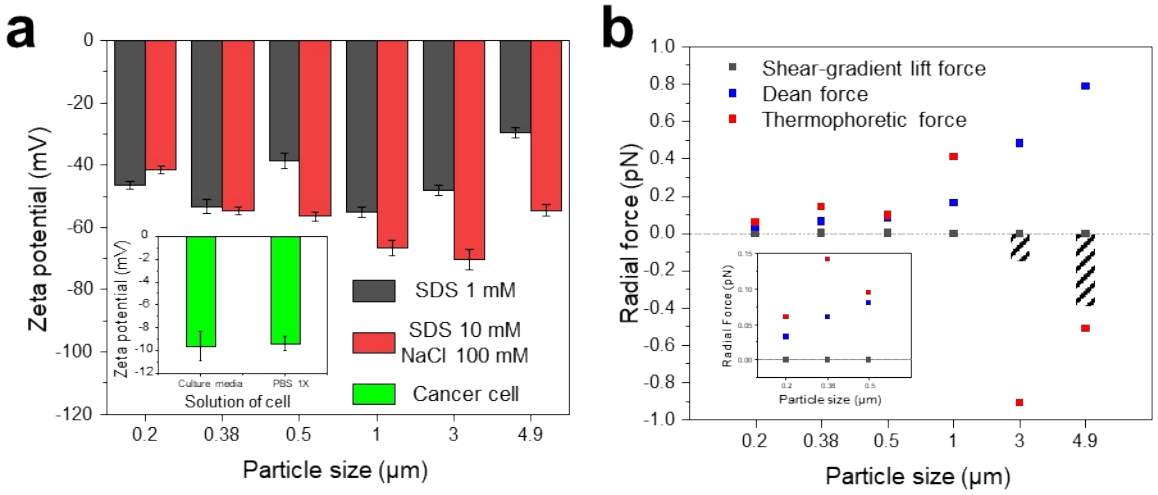

Figure S5. Zeta potential measurement and theoretical analysis of samples. (a) Zeta potentials (ζ) of particles and cells calculated using the Smoluchowski equation based on electrophoretic mobility data obtained from the Zetasizer Nano ZS system. Note: Measurements were performed at 50℃ for particles and at 25℃ (room temperature) for cells. Inset in (a): Zeta potential of Cells in different media. (b) Comparison of forces acting on the particles (Re = 2.14). Inset in (b): An enlarged view of the forces acting on the nanoparticles.

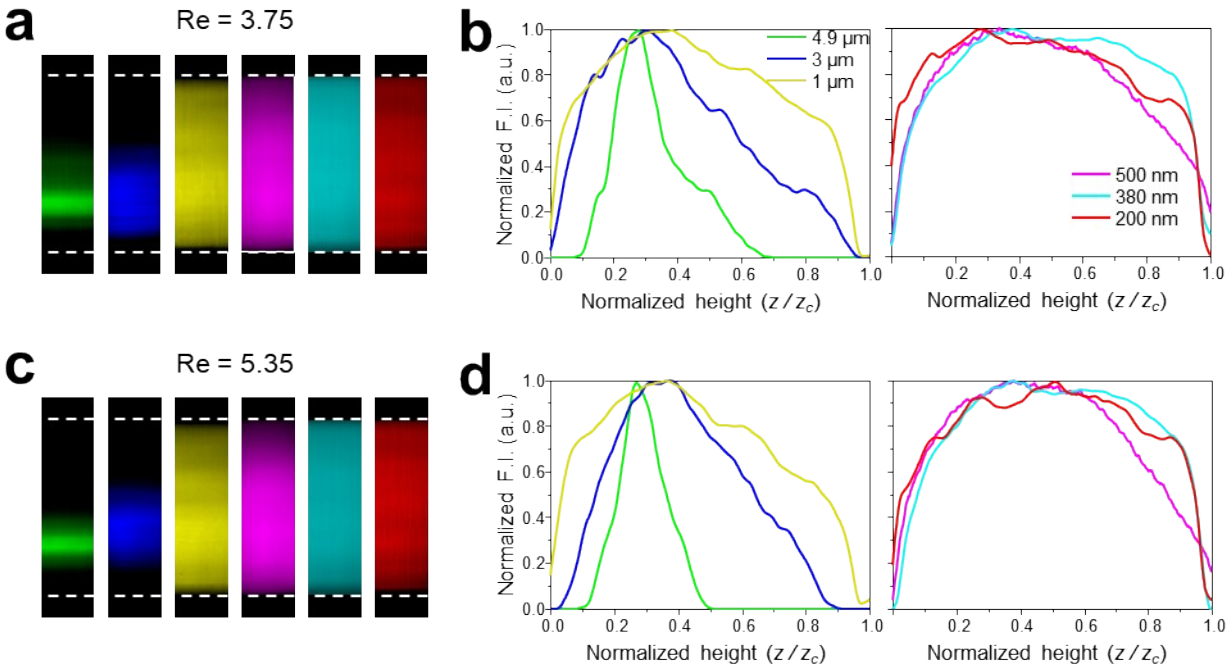

Figure S6. Experimental results of single-size particle suspension for characterization of inertial effect. (a) Fluorescence images of particles with different sizes. (b) Distribution of fluorescence intensity by the inertial effect across micron- and submicron-sized particles when *Re* = 3.75. (c) Fluorescence images of particles with different sizes. (d) Distribution of fluorescence intensity by the inertial effect across micron- and submicron-sized particles when *Re* = 5.35.

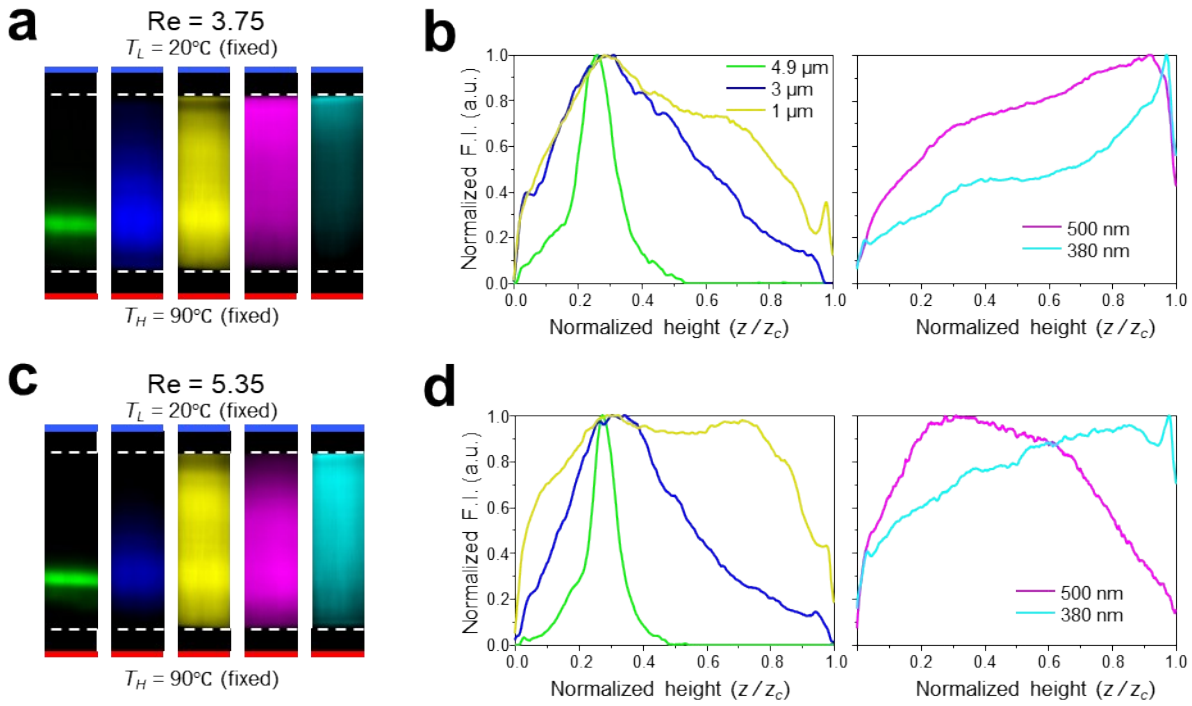

Figure S7. Experimental results of single-size particle suspension for characterization of combined effect. (a) Fluorescence images of particles with different sizes. (b) Distribution of fluorescence intensity due to the combined effect across micron- and submicron-sized particles when *Re* = 3.21. (c) Fluorescence images of particles of different sizes. (d) Distribution of fluorescence intensity by the inertial effect across micron- and submicron-sized particles when *Re* = 5.35.

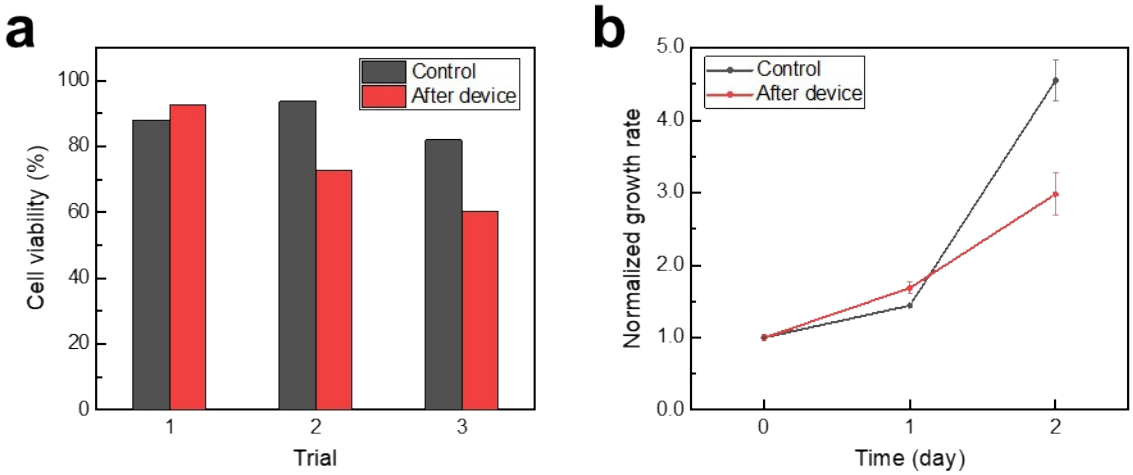

Figure S8. Analysis of cell viability and recovery of single live cell suspensions after processing through the SART device. (a) Comparison of cell viability between K562 cells cultured in T-75 flasks that were either untreated (control) or passed through the device. (b) Growth rate comparison of the two samples after individual cell culture.

Supplementary Tables

Table S1. Benchmarking of the SART device with representative microfluidic separation methods.

Method	Mechanism	Size Range	Resolution	Throughput	Mode	Ref.
Inertial microfluidics	Dean flow + inertial lift	2–20 μm	Moderate	~1 mL/min	Continuous	[9]
Thermophoretic separation	Thermal gradient	0.1–1.0 μm	Low–Moderate	~μL/min	Continuous	[10]
Optofluidic sorting	Photothermal effect	100–500 nm	High	~nL–μL/min	Batch	[11]
Electrokinetic separation	Electro osmotic flow + electrophoresis	100–1000 nm	Moderate	~μL/min	Continuous	[12]
This work (SART device)*	Inertia + thermophoresis	200 nm–5 μm	Moderate–High	~10 μL/min	Continuous	-

* indicates that sheath flow is not involved.

Table S2. COMSOL simulation parameters summary.

Parameter	Value / Description
Working fluid	Water (ρ = 998 kg/m³, μ = 0.89 mPa·s)
Channel width × height	100 μm × 300 μm
Chip material	OSTE+ (κ = 0.2 W/m·K, c_p = 1200 J/kg·K)
Boundary conditions (flow)	Inlet velocity: 0.014 m/s; outlet: pressure 0 Pa
Boundary conditions (thermal)	Heating surface: constant T = 90 °C; cooling surface: constant T = 20°C
Mesh	Free tetrahedral mesh, min size = 3 μm
Physics modules used	Laminar Flow, Heat Transfer in Solids and Fluids, Transport of Diluted Species

References

1. X. Wang, Z. Liu, Y. Yang, Y. Cai, Q. Song and B. Wang, *Chemical Engineering and Processing - Process Intensification*, 2022, **179**, 109057.
2. A. Würger, *Physical Review Letters*, 2008, **101**, 108302.
3. S. Duhr and D. Braun, *Proceedings of the National Academy of Sciences*, 2006, **103**, 19678-19682.
4. Y. Zhou, C. Yang, Y. C. Lam and X. Huang, *International Journal of Heat and Mass Transfer*, 2016, **101**, 1283-1291.
5. S. A. Putnam, D. G. Cahill and G. C. L. Wong, *Langmuir*, 2007, **23**, 9221-9228.
6. D. Di Carlo, D. Irimia, R. G. Tompkins and M. Toner, *Proceedings of the National Academy of Sciences*, 2007, **104**, 18892-18897.
7. A. Würger, *Physical Review Research*, 2020, **2**, 042030.
8. D. Vigolo, R. Rusconi, H. A. Stone and R. Piazza, *Soft Matter*, 2010, **6**, 3489-3493.
9. D. Di Carlo, *Lab on a Chip*, 2009, **9**, 3038-3046.
10. T. Zhang, Z.-Y. Hong, S.-Y. Tang, W. Li, D. W. Inglis, Y. Hosokawa, Y. Yalikun and M. Li, *Lab on a Chip*, 2020, **20**, 35-53.
11. S. Yang and J. C. Ndukaife, *Light: Science & Applications*, 2023, **12**, 188.
12. X. Xuan, *ELECTROPHORESIS*, 2019, **40**, 2484-2513.